

Photodissociation of interstellar ArH⁺

E. Roueff¹, A. B. Alekseyev², and J. Le Bourlot¹

¹ LERMA and UMR 8112, Observatoire de Paris, Place J. Janssen, 92190 Meudon, France
e-mail: evelyne.roueff@obspm.fr

² Fachbereich C, Physikalische und Theoretische Chemie, Bergische Universität Wuppertal, Gaußstrasse 20, D-42097 Wuppertal, Germany
e-mail: alexeev@uni-wuppertal.de

³ LERMA and UMR 8112, Observatoire de Paris, Place J. Janssen, 92190 Meudon, France
e-mail: jacques.lebourlot@obspm.fr

Received ; accepted

ABSTRACT

Aims. Following the recent detection of ³⁶ArH⁺ in the Crab nebula spectrum, we have computed the photodissociation rate of ArH⁺ in order to constrain the physical processes at work in this environment.

Methods. Photodissociation cross sections of ArH⁺ are computed in an *ab initio* approach including explicit account of spin-orbit coupling.

Results. We report the photodissociation cross section of ArH⁺ as a function of wavelength. Photodissociation probabilities are derived for different impinging radiation fields. The photodissociation probability of for a very small unshielded cloud surrounded on all sides by the unshielded InterStellar Radiation Field (ISRF) model described by Draine (1978) is equal to $9.9 \cdot 10^{-12} \text{ s}^{-1}$ and $1.9 \cdot 10^{-9} \text{ s}^{-1}$ in the Crab nebula conditions. The dependence on the visual extinction is obtained by using the Meudon Photon Dominated Region (PDR) code and corresponding analytical fits are provided.

Conclusions. These data will help to produce a realistic chemical network to interpret the observations. Photodissociation of ArH⁺ is found to be moderate and the presence of this molecular ion is mainly dependent on the molecular fraction.

Key words. Molecules – Interstellar -medium – Molecular Physics

1. Introduction

Whereas ArH⁺ has been studied in great detail from laboratory and theoretical techniques, the detection of the ³⁶ArH⁺ isotopologue in the Crab nebula (Barlow et al. 2013) offers an outstanding opportunity to exploit these studies in a previously unforeseen astrophysical context. The main motivation for this article is to investigate the response of this molecular ion to the high ambient radiation field and subsequently check the chemical processes at work in the Crab Nebula environment. Section 2 describes the recent *ab initio* studies of ArH⁺. We use the available information to compute photodissociation rates resulting from different shapes of the incident radiation fields as discussed in Section 3. We first describe the main features of Photon Dominated Regions (PDR) models and introduce different radiation fields to compute the photodissociation probabilities. We summarize our conclusions in Section 4.

2. *Ab initio* study of ArH⁺

The *ab initio* data which are used in the present work to analyze the ArH⁺ photodissociation have been obtained in the detailed theoretical study (Alekseyev et al. 2007) dealing with the computation of molecular potentials and transition moments of the ArH⁺ cation. The multireference spin-orbit CI (Configuration Interaction) method in its $\Lambda - S$ contracted version (LSC-SO-CI) has been used for this purpose. It combines a multireference single- and double-excitation CI approach (MRD-CI) with relativistic effective core potentials (RECP). The LSC-SO-CI

method has been described comprehensively in Alekseyev et al. (2003), while technical details of the ArH⁺ computations have been given in Alekseyev et al. (2007).

The ground X ¹Σ⁺ state of ArH⁺ correlates to the Ar(¹S) + H⁺ asymptote, whereas all low-lying excited electronic states converge to the charge-transfer Ar⁺(²P^o) + H(²S) limit. The computed spectroscopic constants for the X ¹Σ⁺ ground state as well as its dipole moment are found to be in very good agreement with experiments (Johns 1984; Šurkus 2000). While the ArH⁺ ground state is well bound due to the strong argon-proton interaction, the lowest excited states, *b* ³Π, *B* ¹Π (...σ²π³σ*), *a* ³Σ⁺, and *A* ¹Σ⁺ (...σπ⁴σ*) are all repulsive in the Franck–Condon region. They possess very shallow potential minima at large internuclear distances due to the weak attraction between the Ar⁺ cation and hydrogen. The *ab initio* calculations give for the depths of these wells 230–280 cm⁻¹ for most of the triplet states and 60–90 cm⁻¹ in the case of *A* ¹Σ⁺ and *b* ³Π₀⁺.

Computing photodissociation of the ArH⁺ system in realistic conditions requires taking into account the spin-orbit (SO) interaction in the Ar⁺ cation, in which the ²P_{1/2} – ²P_{3/2} splitting is equal to 1431 cm⁻¹ (Saloman 2010), corresponding to an energy of 2060 K. Together with the various potential energy curves converging to the fine structure levels of Ar⁺, Alekseyev et al. (2007) have computed electric dipole moments for transitions to the states responsible for the first absorption continuum (*A* band) of ArH⁺ for the first time in the approach including SO coupling, as well as the corresponding extinction coefficients ϵ expressed in l cm⁻¹ mole⁻¹. It has been shown that the ArH⁺ absorption in the *A* band may be divided into two regions. Its

high-energy part peaking at 123270 cm^{-1} is dominated by the parallel $A^1\Sigma^+ \leftarrow X^1\Sigma^+$ transition, by far the strongest among transitions in this energy range. The low-energy part of the band peaking at 86560 cm^{-1} mainly originates from the perpendicular $B^1\Pi \leftarrow X^1\Sigma^+$ transition, which is ~ 240 times weaker than $A \leftarrow X$ at its maximum. The two partial absorption spectra overlap (equal intensities at around $95 \cdot 10^3 \text{ cm}^{-1}$ corresponding to 1053 \AA), which leads to a shoulder in the red part of the absorption curve. All other transitions in this energy region are spin-forbidden, but it can be noted that absorption into the $b^3\Pi_0^+$ state is not negligible in the $(70 - 80) \cdot 10^3 \text{ cm}^{-1}$ range. It should be possible to detect it from the product angular distribution in the $\text{Ar}^+(^2P_{3/2}) + \text{H}(^2S)$ dissociation channel. The branching ratio Γ for the final photodissociation products has also been calculated and it has been shown that it smoothly increases from 0 in the red tail of the band to 1 at $E \geq 10^5 \text{ cm}^{-1}$. The latter value corresponds to the exclusive formation of the spin-excited $\text{Ar}^+(^2P_{1/2})$ ions, that can lead to the IR laser generation on the $\text{Ar}^+(^2P_{1/2} - ^2P_{3/2})$ transition. All spectral calculations have been carried out for $^{40}\text{ArH}^+$. It is easy to show, however, that the zero-point-energy in the ground state of the $^{36}\text{ArH}^+$ cation increases by $\sim 2 \text{ cm}^{-1}$ with respect to $^{40}\text{ArH}^+$, which is of negligible importance for the present analysis.

In this study, we derive the corresponding photodissociation cross sections from the relation $\sigma = 1000 \times \log_{10}(e) \times \varepsilon/N_A$. ε is the extinction coefficient computed in Alekseyev et al. (2007) expressed in $\text{l mol}^{-1} \text{ cm}^{-1}$ and N_A is the Avogadro number. We thus derive $\sigma = 3.82 \times 10^{-21} \times \varepsilon$, where σ is now in cm^2 . Figure 1 reports the dependence of the dissociation cross section as a function of the wavelength, expressed in \AA . Since all electronically excited potential curves are repulsive, the cross section is continuous and does not display any resonance. The vertical blue dotted line shows the wavelength cutoff at 912 \AA , which takes place in astrophysical media, as all photons are absorbed if their energy is above the ionization potential of atomic hydrogen. The threshold of the total photodissociation cross section occurs at 1500 \AA . The values display a maximum at 800 \AA and become negligible below 670 \AA .

We report the total photodissociation cross section as a function of wavelength in the online material.

3. Photodissociation probabilities

We now consider ArH^+ photodissociation for different impinging radiation fields. As emphasized in van Dishoeck et al. (2006), photodissociation occurs in the surface layers of molecular environments exposed to UV radiation fields. We use the Meudon PDR code facility¹ (Le Petit et al. 2006) to compute the photodissociation probability of ArH^+ for different incident radiation fields as a function of the visual magnitude.

The main feature of the Meudon PDR code is a detailed computation of the radiative transfer of the VUV radiation field in a cloud model containing both gas and dust. Photodissociation of molecular hydrogen is computed from detailed molecular properties of Lyman and Werner transitions as computed by Abgrall et al. (1993, 2000) involving a discrete absorption followed by emission towards the continuum of the X molecular state. Absorption by gas and dust is treated in a consistent way and we refer the reader to the reference paper describing the Meudon PDR code (Goicoechea & Le Boulot 2007; Le Petit et al. 2006).

3.1. Photodissociation in an unshielded environment.

The photodissociation (photoionization) probability of any molecular (atomic) species for a very small parcel of gas surrounded on all sides by the ISRF is expressed as

$$k_{pd}^{cont} = \int_{912}^{\lambda_{max}} \sigma(\lambda) N(\lambda) d\lambda, \quad (1)$$

where $N(\lambda)$ is the number of photons per square centimeter per second and per \AA and $\sigma(\lambda)$ the corresponding cross section. We express this quantity as a function of the radiation energy density via

$$N(\lambda) = \frac{\lambda}{4\pi h} u(\lambda), \quad (2)$$

which is valid for an isotropic incident radiation field. We show in Figure 2 the incident energy densities of three radiation fields which have been used for the computations. We have constrained those radiation fields to contain the same incident integrated energy density for a wavelength range between 912 and 2400 \AA , corresponding to the Habing cutoff of the UV radiation field (Habing 1968). This choice is slightly different from that made by van Dishoeck et al. (2006), who have used a cutoff of 2050 \AA .² The model using the incident Draine radiation field is defined as the standard case.

The radiation field impinging the molecular knots where ArH^+ has been detected (Barlow et al. 2013) may be estimated as well. The pulsar wind nebula (PWN) luminosity is obtained from a dust + photoionization modeling of the Crab nebula by Owen and Barlow (2014)³ using the spectrum displayed in Hester (2008). The integrated PWN luminosity is $1.3 \times 10^{38} \text{ erg/s}$ and is assumed to be emitted from the central two-thirds of the ellipsoidal nebula, whose overall dimensions are adopted to be $3.8\text{pc} \times 2.9 \text{ pc}$. Table 2 displays the photodissociation rate (P_d) of ArH^+ as well as the photoionization probability (P_i) of atomic carbon computed from the direct integration in equation 1 for the three chosen radiation fields and for the crab nebula environment. We also display the ratios of the radiation field energy densities to that corresponding to the Draine radiation field in the $911 - 2400 \text{ \AA}$ window. The results concerning photoionization of carbon given by van Dishoeck et al. (2006) are also reported. The differences obtained reflect the different choice of normalization of the radiation fields. The value displayed for the Crab nebula is about two hundred times larger than in standard interstellar conditions and the ratio of the corresponding energy densities is about 80.

3.2. Role of the dusty environment

We consider now a cloud irradiated on one side and we follow the decrease of the radiation field as it penetrates inside the molecular cloud. This reduction is a result of photon absorption both by gas and dust. Dust absorption and scattering properties are introduced, using the prescription by Weingartner & Draine (2001) for the Milky Way for spherical dust particles with radii between 0.3μ and 3 nm following a -3.5 power law of the dust size distribution (Mathis et al. 1977). Dust absorption is a continuum process as well as gas phase absorption by ArH^+ , as shown in Figure 1. We also recall that such a

² We have verified that we obtain identical results for carbon photoionization in that case.

³ Owen P., Barlow M.J., in preparation

¹ available at <http://pdr.obspm.fr>

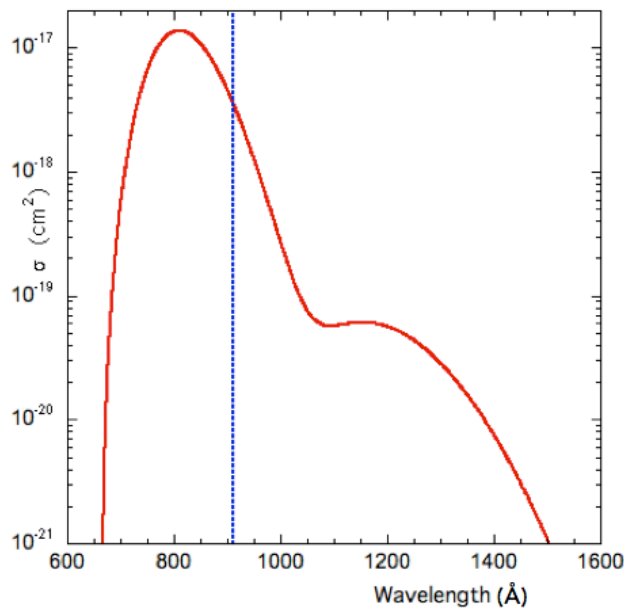


Fig. 1. Total photodissociation cross section of ArH⁺ as a function of incident wavelength in Å. The vertical blue dotted line represents the wavelength cutoff of the interstellar radiation field

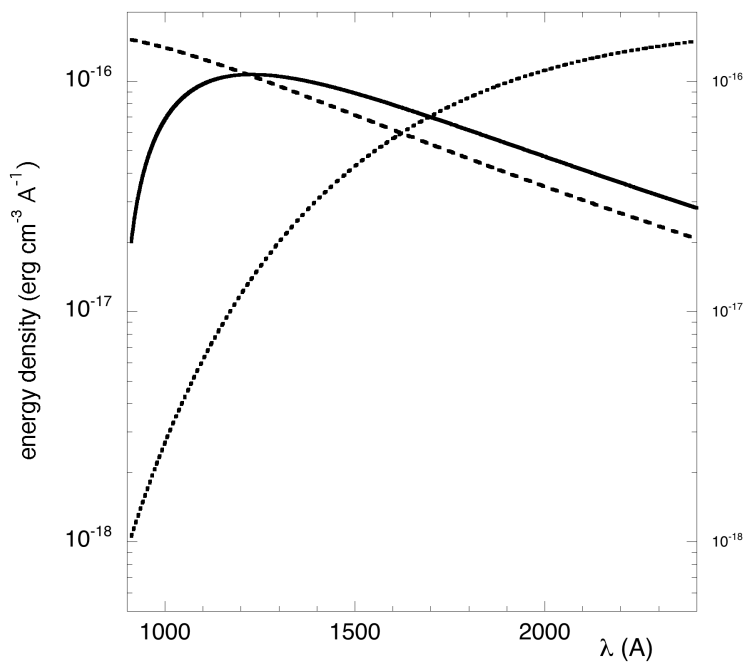


Fig. 2. Energy density of the radiation fields as a function of wavelength. Solid line: Draine, dotted line: black body at T=10,000K, dashed line: black body at T=37,000K.

continuum mechanism occurs in the photoionization of carbon as the corresponding cross section is constant from $I_C = 11.26$ eV (corresponding to 1101.5 Å), equal to $1.6 \cdot 10^{-17}$ cm² up to 13.6 eV. An exponential decrease is often used to represent the A_V dependence of the photoprocesses and the corresponding parameters are found in the different kinetic databases (KIDA (<http://kida.obs.u-bordeaux1.fr>) (Wakelam et al. 2012), UDFA (<http://www.udfa.net>) (McElroy et al. 2013)). These expressions are aimed to describe the effect of dust continuum absorption on the photoionization and photodissociation probabilities. We

consider a cloud model with a proton density $n_H = 10^3$ cm⁻³ and submitted to a cosmic ionization rate of $5 \cdot 10^{-17}$ s⁻¹, corresponding to standard translucent cloud conditions. The radiation, impinging isotropically on one side of a semi-infinite slab, is described by the Draine analytic ISRF model (Draine 1978). We display as full lines in Figure 3 the computed ArH⁺ photodissociation and Carbon photoionization probabilities as a function of A_V . The corresponding exponential fits are displayed as dotted lines in the left hand part (a) of Figure 3 for a restricted visual extinction range between 0 and 3, as recommended in van

Dishoeck et al. (2006). We also display in the right hand part (b) of Figure 3, as dotted lines, the corresponding fitting functions using the exponential integral E_2 function. Whereas the exponential dependence is a fair approximation of the photodissociation probabilities for the considered range of visual extinctions, the fit using the E_2 function is superior as already emphasized and used in Neufeld & Wolfire (2009). Corresponding formulae are displayed in Table 3.

We also compute the photodissociation rate resulting from radiating stars, considered as the blackbodies already introduced in Section 3.1 and displayed in Figure 2, where the radiation is considered as beamed perpendicularly to the surface of the cloud, which corresponds to regions located close to a particular star. In those cases, exponential fits are found to be adequate representations of the visual extinction A_V dependence of the photodissociation rates, as shown in Figure 4. Finally, we also compute the photodissociation probability corresponding to the Crab nebula conditions where the radiation is isotropic. We assume a proton density $n_H = 2 \times 10^4 \text{ cm}^{-3}$ representative of the molecular knots detected by Loh et al. (2012) in this environment. The corresponding results are displayed in Figure 4 and fitting expressions are given in Table 3. The constant factors expressed in s^{-1} are about one half the value given for the unshielded case (Table 2) as the radiation is impinging on one single side of the cloud.

3.3. Role of the continuous gas phase absorption

However, these analytic representations of photodissociation/photoionization probabilities neglect the role of other gas phase continuum absorptions. Reemphasizing early PDR models by Tielens & Hollenbach (1985), Rollins & Rawlings (2012) have pointed out recently that neglecting mutual shielding by dust and carbon leads to overestimate the photoionization probability of Carbon by a factor $\exp(-\sigma_C N_C)$, where σ_C is the photoionization cross section of Carbon and N_C stands for the column density of atomic Carbon. We investigate in Figure 5 the role of additional gas phase absorption for the standard model case, where we introduce the photodissociation and photoionization continuous cross sections of different gas phase compounds, including Carbon. The solid line curves correspond to models including continuous absorption of the radiation field by gas whereas dotted lines curves correspond to computations neglecting that effect. Whereas gas phase absorption considerably modifies the photoionization probability A_V dependence for Carbon, the effect on ArH^+ photodissociation is much less significant as the photodissociation threshold is at 1500 \AA , at a significantly larger wavelength than for Carbon photoionization (1105 \AA).

3.4. Relevance to the Crab environment

The main chemical processes involved in the formation/destruction of ArH^+ , except photodissociation, have been discussed in Barlow et al. (2013). The availability of the photodissociation cross sections allows to constrain further the chemical processes at work. The chemical network is relatively simple as displayed in Figure 6. The initial step of the chemistry is ionization of Argon through cosmic rays and X-rays followed by a reaction with molecular hydrogen. An alternative path is provided by the reaction between H_2^+ with neutral Argon. The abundance of ArH^+ is thus directly proportional to the total ionization rate of Ar. The ionization state of Ar is discussed

by Jenkins (2013) in the context of the Warm Neutral Medium (WNM) and non conventional sources of ionization are proposed to reconcile a $[\text{ArI} / \text{OI}]$ ratio that is consistent both with the observations and the generally accepted value of the density $n(\text{HI}) = 0.5 \text{ cm}^{-3}$. It is interesting to note that the molecular OH^+ ion, which is recognized to be a test of cosmic ionization rate (Indriolo 2013), has been detected in the same environment (Barlow et al. 2013). A quantitative study is beyond the scope of the present paper and a realistic study would require the introduction of the X ray spectrum. The photodissociation rate of ArH^+ at the surface of the molecular knots is computed to be about $2 \cdot 10^{-9} \text{ s}^{-1}$ which may compete with dissociative recombination (with corresponding rate constant $k_e \leq 5 \times 10^{-8} \text{ cm}^3 \text{ s}^{-1}$ (Mitchell et al. 2005)). However reactions with molecular hydrogen (with a rate \sim to $2 \times 10^{-9} \text{ cm}^3 \text{ s}^{-1}$ (Anicich 2003)) are presumably the main destruction channel.

4. Summary

We report photodissociation cross sections of ArH^+ as a function of wavelength which can be used to compute the response of that molecular ion to ultraviolet interstellar radiation fields. The photodissociation rate of ArH^+ for a very small unshielded cloud surrounded on all sides by the standard Draine UV ISRF is $9.9 \cdot 10^{-12} \text{ s}^{-1}$. This value is very sensitive to the spectral distribution in the VUV 911 - 2400 \AA wavelength window, as shown in Table 2. The corresponding rate relevant to the Crab nebula environment is $1.9 \cdot 10^{-9} \text{ s}^{-1}$. The dependence on the visual extinction A_V due to the attenuation of radiation by dust is derived from the Meudon PDR code both for incident isotropic and plane parallel radiations. We report the corresponding analytic functions for a semi infinite plane parallel cloud for different typical cases and for the Crab nebula environment. The constant numerical factor is close to half the value obtained for the unshielded environment. The dependence on A_V is better represented with an E_2 function when isotropic radiation is impinging on the cloud. Nevertheless, we stress out that a direct integration of the product of photodissociation cross sections by the actual radiation field allows to derive photo destruction rates unambiguously. The actual value of the photodissociation rate is moderate and destruction of ArH^+ is mainly due to molecular H_2 . Then, ArH^+ , as well as OH^+ also detected in the Crab nebula (Barlow et al. 2013), are strongly dependent on the molecular fraction of the gas.

Acknowledgements. We thank M.J. Barlow for various informations on the Crab nebula environment. After the refereeing process of the paper, we have been aware of an additional detection of ArH^+ in the diffuse ISM (Schilke et al. 2014). We thank particularly D. Neufeld and J.H. Black for helpful exchanges and related informations. ER and JLB thank support from the CNRS National Program PCMI (Physico-Chimie du Milieu Interstellaire). ABA acknowledges support from the Deutsche Forschungsgemeinschaft.

References

- Abgrall, H., Roueff, E., & Drira, I. 2000, A&AS, 141, 297
- Abgrall, H., Roueff, E., Launay, F., Roncin, J. Y., & Subtil, J. L. 1993, Journal of Molecular Spectroscopy, 157, 512
- Alekseyev, A. B., Liebermann, H.-P., & Buenker, R. J. 2003, in Recent advances in Relativistic Effects in Chemistry, ed. K. Hirao & Y. Ishikawa (Singapore: World Scientific), 65
- Alekseyev, A. B., Liebermann, H.-P., & Buenker, R. J. 2007, Physical Chemistry Chemical Physics (Incorporating Faraday Transactions), 9, 5088
- Anicich, V. G. 2003, An Index of the Literature for Bimolecular Gas Phase Cation-Molecule Reaction Kinetics, Tech. rep., JPL Publication 03-19
- Barlow, M. J., Swinyard, B. M., Owen, P. J., et al. 2013, Science, 342, 1343
- Draine, B. T. 1978, ApJS, 36, 595
- Goicoechea, J. R. & Le Boulouet, J. 2007, A&A, 467, 1

- Habing, H. J. 1968, *Bull. Astron. Inst. Netherlands*, 19, 421
- Hester, J. J. 2008, *A&A*, 46, 127
- Indriolo, N. 2013, in *Advances in Solid State Physics*, Vol. 34, *Cosmic Rays in Star-Forming Environments*, ed. D. F. Torres & O. Reimer, 83
- Jenkins, E. B. 2013, *ApJ*, 764, 25
- Johns, J. W. C. 1984, *Journal of Molecular Spectroscopy*, 106, 124
- Le Petit, F., Nehmé, C., Le Bourlot, J., & Roueff, E. 2006, *ApJS*, 164, 506
- Loh, E. D., Baldwin, J. A., Ferland, G. J., et al. 2012, *MNRAS*, 421, 789
- Mathis, J. S., Rimpl, W., & Nordsieck, K. H. 1977, *ApJ*, 217, 425
- McElroy, D., Walsh, C., Markwick, A. J., et al. 2013, *A&A*, 550, A36
- Mitchell, J. B. A., Novotny, O., LeGarrec, J. L., et al. 2005, *Journal of Physics B Atomic Molecular Physics*, 38, L175
- Neufeld, D. A. & Wolfire, M. G. 2009, *ApJ*, 706, 1594
- Rollins, R. P. & Rawlings, J. M. C. 2012, *MNRAS*, 427, 2328
- Saloman, E. B. 2010, *Journal of Physical and Chemical Reference Data*, 39, 033101
- Schilke, P., Neufeld, D. A., Mueller, H. S. P., et al. 2014, *ArXiv e-prints*
- Tielens, A. G. G. M. & Hollenbach, D. 1985, *ApJ*, 291, 722
- Šurkus, A. 2000, *Spectrochimica Acta Part A: Molecular Spectroscopy*, 56, 1979
- van Dishoeck, E. F., Jonkheid, B., & van Hemert, M. C. 2006, *Faraday Discussions*, 133, 231
- Wakelam, V., Herbst, E., Loison, J.-C., et al. 2012, *ApJS*, 199, 21
- Weingartner, J. C. & Draine, B. T. 2001, *ApJ*, 548, 296

Table 2. Photodissociation rates computed for an unshielded environment. VD06 refers to van Dishoeck et al. (2006).

Radiation field	ratio of energy densities	Pd(ArH ⁺) (s ⁻¹)	Pi(C) (s ⁻¹)	
			present result	VD06
Draine	1	9.9×10^{-12}	3.1×10^{-10}	3.1×10^{-10}
Black body of 10000K	1	7.0×10^{-13}	1.7×10^{-11}	2.5×10^{-11}
Black body of 37000K	1	3.7×10^{-11}	7.6×10^{-10}	
Crab nebula	83.9	1.9×10^{-9}	4.1×10^{-8}	

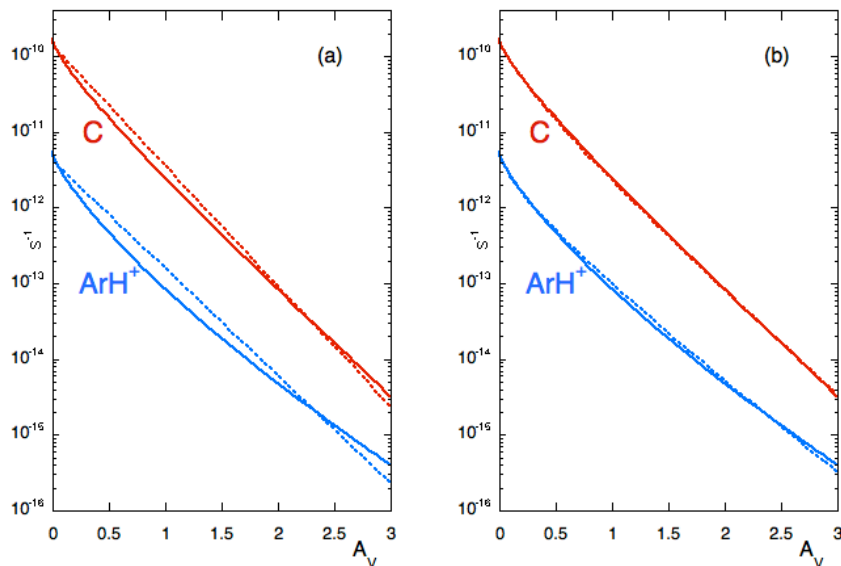

Fig. 3. Computed photodissociation and photoionization rates of ArH⁺ (blue) and C (red) at the surface of a semi-infinite slab for a Draine isotropic ISRF. Full lines correspond to PDR model results and dotted lines display the analytical fits : (a) exponential; (b) E₂ function.

Table 3. Fitting functions of the photodissociation rate of ArH⁺ and photoionization rate of Carbon as functions of the visual magnitude for the different radiation fields used in Table 2. IS and PP stand respectively for isotropic and perpendicular irradiation.

Radiation field	Pd(ArH ⁺) (s ⁻¹)	Pi(C) (s ⁻¹)
IS Draine	$4.2 \times 10^{-12} \times \exp(-3.27 A_V)$	$1.40 \times 10^{-10} \times \exp(-3.67 A_V)$
IS Draine	$4.84 \times 10^{-12} \times E_2(2.46 A_V)$	$1.78 \times 10^{-10} \times E_2(2.84 A_V)$
PP BB 10,000K	$3.54 \times 10^{-13} \times \exp(-2.28 A_V)$	$8.91 \times 10^{-12} \times \exp(-2.99 A_V)$
PP BB 37,000K	$1.56 \times 10^{-11} \times \exp(-3.04 A_V)$	$3.83 \times 10^{-10} \times \exp(-3.14 A_V)$
IS Crab	$9.66 \times 10^{-10} \times E_2(2.83 A_V)$	$2.29 \times 10^{-8} \times E_2(2.93 A_V)$

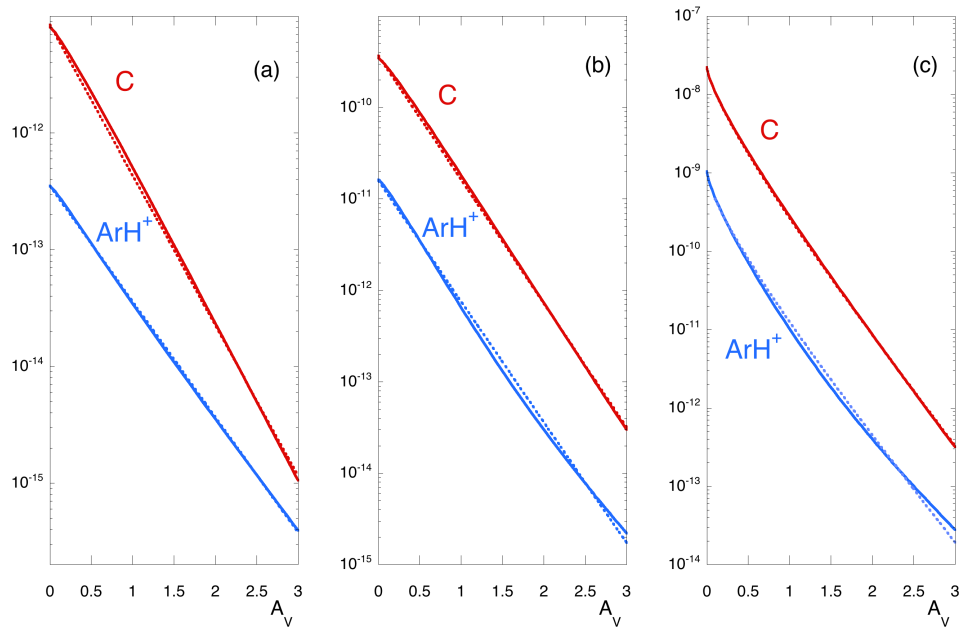


Fig. 4. Computed photodissociation and photoionization rates of ArH⁺ (blue) and C (red) at the surface of a semi-infinite slab as a function of visual extinction A_V . Full lines correspond to PDR model results and dotted lines display the fit equations results, as given in Table 3. (a) (b) and (c) represent the BB 10,000 K, BB 37,000 K and the Crab nebula cases.

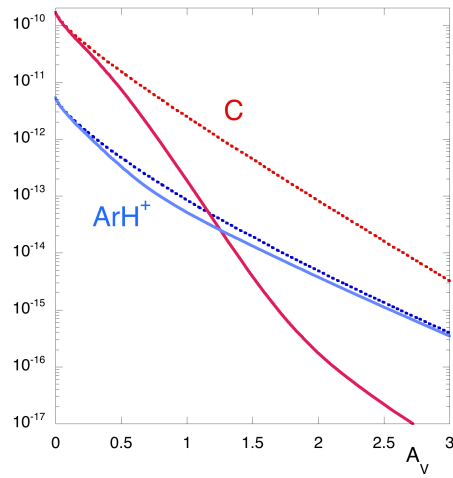


Fig. 5. Computed photodissociation and photoionization rates of ArH⁺ (blue curves) and C (red curves) at the surface of a semi-infinite slab for the Draine radiation field; solid line: PDR model including continuous dust + gas phase absorption; dotted line: PDR model with continuous dust absorption only.

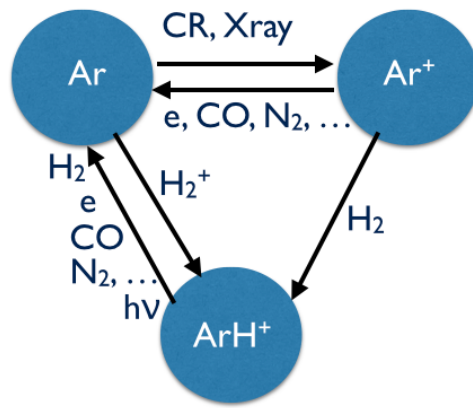


Fig. 6. Chemical network of the ArH⁺ molecular ion.

Table 1. Photodissociation cross section of ArH⁺ as a function of wavelength in Å.

Wavelength Å	Photodissociation cross section cm ²
6.667e+02	6.880e-22
6.681e+02	1.595e-21
6.690e+02	2.629e-21
6.702e+02	4.370e-21
6.711e+02	6.165e-21
6.720e+02	8.366e-21
6.740e+02	1.499e-20
6.790e+02	4.382e-20
6.802e+02	5.348e-20
6.851e+02	1.109e-19
6.900e+02	2.033e-19
6.951e+02	3.410e-19
6.970e+02	4.080e-19
6.980e+02	4.446e-19
7.002e+02	5.363e-19
7.041e+02	7.334e-19
7.081e+02	9.772e-19
7.101e+02	1.117e-18
7.121e+02	1.271e-18
7.149e+02	1.505e-18
7.170e+02	1.695e-18
7.180e+02	1.796e-18
7.201e+02	2.009e-18
7.230e+02	2.328e-18
7.240e+02	2.450e-18
7.280e+02	2.942e-18
7.330e+02	3.645e-18
7.352e+02	3.973e-18
7.390e+02	4.580e-18
7.401e+02	4.760e-18
7.420e+02	5.081e-18
7.450e+02	5.596e-18
7.470e+02	5.936e-18
7.490e+02	6.284e-18
7.501e+02	6.486e-18
7.520e+02	6.849e-18
7.555e+02	7.480e-18
7.560e+02	7.583e-18
7.580e+02	7.949e-18
7.630e+02	8.824e-18
7.700e+02	1.005e-17
7.760e+02	1.101e-17
7.790e+02	1.144e-17
7.820e+02	1.184e-17
7.870e+02	1.243e-17
7.910e+02	1.286e-17
7.970e+02	1.332e-17
8.002e+02	1.348e-17
8.102e+02	1.373e-17
8.145e+02	1.370e-17
8.192e+02	1.355e-17
8.260e+02	1.318e-17
8.304e+02	1.287e-17
8.360e+02	1.238e-17
8.402e+02	1.193e-17
8.452e+02	1.136e-17
8.502e+02	1.076e-17
8.560e+02	1.002e-17
8.590e+02	9.634e-18

Table 1. Continued.

Wavelength Å	Photodissociation cross section cm ²
8.702e+02	8.148e-18
8.751e+02	7.518e-18
8.860e+02	6.154e-18
8.903e+02	5.650e-18
8.951e+02	5.126e-18
8.991e+02	4.710e-18
9.003e+02	4.588e-18
9.052e+02	4.110e-18
9.060e+02	4.034e-18
9.081e+02	3.843e-18
9.102e+02	3.660e-18
9.106e+02	3.624e-18
9.110e+02	3.589e-18
9.202e+02	2.871e-18
9.301e+02	2.229e-18
9.401e+02	1.696e-18
9.504e+02	1.271e-18
9.600e+02	9.565e-19
9.702e+02	7.010e-19
9.802e+02	5.149e-19
9.904e+02	3.723e-19
9.953e+02	3.187e-19
1.000e+03	2.729e-19
1.005e+03	2.338e-19
1.010e+03	2.033e-19
1.015e+03	1.743e-19
1.020e+03	1.523e-19
1.025e+03	1.319e-19
1.030e+03	1.167e-19
1.035e+03	1.026e-19
1.040e+03	9.214e-20
1.045e+03	8.351e-20
1.050e+03	7.651e-20
1.055e+03	7.105e-20
1.060e+03	6.681e-20
1.063e+03	6.456e-20
1.067e+03	6.238e-20
1.070e+03	6.108e-20
1.073e+03	6.001e-20
1.077e+03	5.887e-20
1.080e+03	5.826e-20
1.083e+03	5.776e-20
1.087e+03	5.738e-20
1.090e+03	5.722e-20
1.093e+03	5.715e-20
1.097e+03	5.719e-20
1.100e+03	5.730e-20
1.110e+03	5.791e-20
1.120e+03	5.883e-20
1.130e+03	5.974e-20
1.140e+03	6.036e-20
1.150e+03	6.078e-20
1.160e+03	6.081e-20
1.170e+03	6.032e-20
1.180e+03	5.948e-20
1.190e+03	5.814e-20
1.200e+03	5.646e-20
1.220e+03	5.210e-20
1.240e+03	4.679e-20
1.260e+03	4.076e-20

Table 1. Continued.

Wavelength Å	Photodissociation cross section cm ²
1.280e+03	3.453e-20
1.299e+03	2.880e-20
1.300e+03	2.855e-20
1.320e+03	2.308e-20
1.340e+03	1.806e-20
1.360e+03	1.384e-20
1.380e+03	1.041e-20
1.400e+03	7.560e-21
1.420e+03	5.398e-21
1.441e+03	3.721e-21
1.461e+03	2.519e-21
1.490e+03	1.361e-21
1.510e+03	8.606e-22
1.521e+03	6.746e-22
1.530e+03	5.386e-22
1.550e+03	3.234e-22
1.571e+03	1.862e-22
1.591e+03	1.059e-22
1.599e+03	7.594e-23